Green Chemistry

Accepted Manuscript

ROYAL SOCIETY OF CHEMISTRY

www.rsc.org/greenchem

$Fe_{1-x}S$/C nanocomposites from sugarcane waste-derived microporous carbon for high-performance lithium ion batteries

Chundong Wang,[abc] Minhuan Lan,[c] Yi Zhang,[d] Haidong Bian,[c] Muk-Fung Yuen,[c] Kostya (Ken) Ostrikov,[ef] Jianjun Jiang,[a] Wenjun Zhang,[c] Yang Yang Li[c*] and Jian Lu[b*]

[a] *School of Optical and Electronic Information, Huazhong University of Science and Technology, Wuhan 430074, P.R. China*

[b] *Department of Mechanical and Biomedical Engineering, City University of Hong Kong, Hong Kong SAR, P.R. China*

[c] *Center of Super-Diamond and Advanced Films (COSDAF), Department of Physics and Materials Science, City University of Hong Kong, Hong Kong SAR, P.R. China*

[d] *School of Chemical Engineering and Pharmacy, Wuhan Institute of Technology, Wuhan, 430073, P.R. China*

[e] *School of Chemistry, Physics and Mechanical Engineering, Queensland University of Technology, Brisbane, Queensland 4000, Australia*

[f] *Plasma Nanoscience, Industrial Innovation Program, CSIRO Manufacturing Flagship, Lindfield, New South Wales 2070, Australia*

Author to whom correspondence should be addressed. E-mail: yangli@cityu.edu.hk (Y.Y. Li), jianlu@cityu.edu.hk (J. Lu)

† Electronic supplementary information (ESI) available. See DOI: XXX

We report a novel strategy to collect microporous carbon from disposable sugarcane waste for lithium ion battery (LIB) applications. First boiled in water and ethanol and then calcined, the sugarcane waste successfully transforms to microporous carbon, delivering a specific capacity of 311 mAh g^{-1} at 0.33C as the LIB anode materials. For improved LIB performance, pyrrhotite-5T $Fe_{1-x}S$ nanoparticles was uniformly dispersed and robustly attached to the scaffold of the microporous carbon using a novel sulfurization method. A remarkably ultrahigh capacity of 1185 mAh g^{-1} (well beyond theoretical value by 576 mAh g^{-1}) was achieved after 200 charging/discharging cycles at the current density of 100 mA g^{-1}, suggesting the desirable synergetic effects between Fe_{1-x} S and microporous carbon which lead to shortened lithium ion transportation path, enhanced conductivity and effective prevention of polysulfide dissolution. Our approach opens a convenient route for mass-producing sustainable superior LIB electrodes from natural wastes that can substitute commercial graphite.

Introduction

Alarmed by global warming and energy crisis, intensive efforts have been devoted for developing sustainable energy technologies (solar, wind, geothermal and tidal energy).[1] Among different energy storage systems for effectively storing the intermittent natural energy sources, rechargeable lithium ion batteries are one of the most promising candidates.[2-4] For example, they are particularly appealing for portable electronic devices and hybrid electric vehicles (HEVs) due to their high energy density (high voltage joined with high specific capacity, typically at 150 Wh/kg and 650 Wh/l), high rate capability, and long lifespan.[5-8] Nevertheless, the high price of the LIBs largely restricted their wide application, particularly in HEVs, making the development of HEV-based green transportation unrealistic. In fact,

how to effectively lower the manufacturing cost, enhance the safety, increase the lifetime, and improve the energy density are the major challenges of LIBs presented to scientists.[9, 10] Currently, the anode materials of commercial LIBs heavily relies on graphite, which mainly stems from the natural graphite mines and possesses low energy capacities, imposing environmental stress with the threat of depleting the natural graphite reserves to meet the future huge demands from the electric vehicle and electricity grid industries. It is therefore an urgent task for scientists to discover new renewable electrode materials that are environment friendly, cheap and with nearly infinite abundance in nature.[10, 11]

Sugarcane as a popular type of fruit is widely grown in tropical and subtropical regions. Brazil is the largest producer of sugarcane in the world, followed by the next five major producers of India, China, Thailand, Pakistan and Mexico. As estimated by the Food and Agriculture Organization of the United Nations, sugarcane is cultivated on ~ 26.0 million hectares all over the world, in more than 90 countries, producing a worldwide harvest of 1.83 billion tons.[12] It needs to point out that ~60% commercial sugar comes from sugarcane. Notably, after draining the juice, the sugarcane trunks are normally discarded, resulting in a huge amount of bio-waste (up to ~ 223 million tons/year) that needs to be disposed, usually through either direction combustion or landfills for biodegradation that generates air pollution.[13] The direct combustion treatment inevitably emits nitrogen oxides (NO_X), carbon monoxide (CO), CO_2, and sulfur oxides (SO_X),[14] which also makes a main contributor to the haze weather seen recently in China.[15] The landfill treatment could be a more suitable way, but entails large economic consumption. Thus, a more convenient and environmental friendly approach that can effectively convert the huge amount of disposable sugarcane waste into useful commercial products would be highly desirable. Note that the nano-porous activated

carbon[16] and hierarchically porous carbon monoliths[17] have been obtained by from sugarcane waste for supercapacitor applications. Nonetheless, the application of the sugarcane waste-derived microporous carbon for lithium-ion batteries has not been reported.

Herein, we report a new convenient mass-production strategy to convert sugarcane waste into microporous carbon for lithium-ion batteries. Following a simple boiling procedure in water and alcohol, the sugarcane waste was carbonized to be converted into microporous carbon (MC), which was then further coated with $Fe_{1-x}S$ nanoparticles through a novel and facile sulfurization method. When applied as LIB anode materials, the hierarchical $Fe_{1-x}S$-microporous carbon ($Fe_{1-x}S$-MC) nanocomposites thus obtained displayed superior electrochemical performance with ultrahigh specific capacities and excellent cycling stability (1185 mAg^{-1} after 200 cycles), representing the best electrochemical performance among all the iron sulfide-based anode materials reported to date. The success in converting disposable sugarcane to advanced carbon-based materials opens a new route to substitute graphite as electrode materials, unveiling the great potential values of bio-wastes for practical applications.

Experimental

Synthesis of $Fe_{1-x}S$-MC nanocomposites

The schematic illustration of the synthesis process of $Fe_{1-x}S$-MC nanocomposites is depicted shown in Figure 1. Sugarcane trunks disposed from a juice extractor machine were collected from a fruit store in Sham Shui Po, Hong Kong. The sugarcane trunks were cut into pieces and boiled in di-ionized (DI) water and ethanol for 6 hr, respectively, to remove the sugar contents. During each cooking process, it needs to change the fresh solution for one time. After dried in an oven at 90 ^{o}C, the sample was carbonized at 1000 ^{o}C in Ar with a flow rate

of 30 sccm for 4 hr, and cooled down naturally. Microporous carbon (MC) was obtained. For surface functionalization, the MC was treated in a mixture of H_2SO_4 (98%) and HNO_3 (70%) (3:1 by volume) under constant stirring at 110 ^oC for 15 min. The reaction mixture was then filtered with the precipitates washed with DI water for several times.

The aqueous suspension of MC was produced by ultrasonicating 20 mg MC in DI water for 10 min. In a 50 ml Teflon-lined stainless steel autoclave, ~ 40 ml suspension solution and 0.8 g ferric citrate ($FeC_6H_5O_7$) were added. The sealed Teflon-lined autoclave was kept in an oven at 200 ^oC for 18 hr and then cooled down to room temperature naturally. The as-synthesized black precipitate was centrifugally washed with DI water and alcohol for several times, and dried at 100 ^oC, which is denoted as the precursor of our final product. The precursor was then mixed with sulfur powder and subsequently thermally treated under the protection of Ar flow (flow rate: 30 sccm) to generate the final product of $Fe_{1-x}S$-MC. The temperature was first raised at a heating rate of 5 ^oC /min to 149 ^oC, stayed at 149 ^oC for 3 hrs, further raised at 10 ^oC/min to 800 ^oC, and stayed at 800 ^oC for 5 hrs.

Samples characterization

The morphology, crystalline structure and composition of the samples were checked by scanning electron microscope (SEM, Philips XL-30 FESEM), energy dispersive X-ray spectroscopy (EDX, AMETEX), transmission electron microscope (TEM, CM 20 FEG operated with an accelerating voltage of 200 kV), and X-ray photoelectron spectroscopy (XPS, VG ESCALAB 220i-XL surface analysis system equipped with a monochromatic Al-Kα X-ray source of 1486.6 eV). The crystallography was examined with an X-ray diffractometer (XRD, Philips X'Pert MRD with Cu-Kα radiation). Thermogravimetric analysis (TGA) was carried out on a TGA Q50 instrument in air with a heating rate of 10 ^oC/min from ambient

temperature to 800 ^{o}C to determine the percentage of $Fe_{1-x}S$ in the composites. Raman spectral analyses were performed with a Renishaw visual Raman microscope using a 514 nm laser beam with a spectral resolution of 1 cm^{-1} and spatial resolution of approximately 1 mm. The Brunauer–Emmett–Teller (BET) surface area was measured using a Quantachrome surface area analyzer (NOVA 1200).

Electrochemical performance evaluation

The electrochemical performance of $Fe_{1-x}S$-MC was evaluated with LIR2032 coin-type half-cells assembled in an argon-filled glove box (MBraun Lab Master 130). The working electrodes were prepared by mixing the active materials ($Fe_{1-x}S$-MC, or $Fe_{1-x}S$), carbon black (Super-P), and sodium alginate (CMC) with a weight ratio of 80:10:10, and pasting the mixture slurry of 200 μm thick on copper foil (99.6%) using a plastic blade. Pure Li foil was used as the counter electrode and a Celgard 2400 microporous polypropylene membrane was utilized as the separator. A solution of $LiPF_6$ (1.0 $molL^{-1}$) in a mixture of ethylene carbonate (EC)/dimethyl carbonate (DMC)/diethyl carbonate (DEC) (1:1:1, by volume) was applied as the electrolyte. The electrochemical performance of rating and cycling was tested in the voltage range of 0.01 - 3.00 V *vs*. Li/Li^{+} at room temperature. The cyclic voltammetric (CV) measurements were carried out using an electrochemical workstation (CHI, 600D) at a scan rate of 0.1 mV s^{-1} in the range of 0.01 - 3.00V. Electrochemical impedance spectra (EIS) were collected after a 2 h rest by providing an ac voltage of 5 mV amplitude over a frequency range from 100 kHz to 10 mHz within an electrochemistry workstation (Zahner Cimps).

Results and discussion

The SEM study (Fig. 2a-d) of the MC sample collected after the carbonization treatment reveals that a microporous structure was formed featuring a bamboo-like interconnected 3D porous networks with periodic structural features. Further magnified SEM images (Fig. 2b) shows that the pore diameter was ~ 2 - 5 μm. The walls of the microporous carbon was observed to be very thin (Fig. S1) with a sharp edge, suggesting its good mechanical flexibility. A low-magnification SEM image of the microporous carbon (Fig. 2d) shows an array of self-aligned micro-bamboos. Interestingly, the $Fe_{1-x}S$-MC composites possessed an interesting morphology with the self-aligned micro-bamboo tubes decorated with nanoparticles (Fig. 2e-d) which were found to be $Fe_{1-x}S$ nanoparticles from the TEM examination (Fig. 3). A zoomed-in view (Fig. 2e) discloses the regular shape of the Fe_{1-x} S nanoparticles and they were fairly thickly dotted and tightly anchored onto the microporous carbon walls. The specific surface areas of MC and $Fe_{1-x}S$-MC were evaluated to be 110.8 m^2 g^{-1} and 56.7 m^2 g^{-1}, respectively (Fig. S2). To examine the spatial distribution of the Fe_{1-x} S nanoparticles, EDS elemental mapping was performed (Fig. S3). The C (red), Fe (yellow), and S (blue) elements were found to be evenly distributed over the entire measured region, indicating that the uniform distribution of the $Fe_{1-x}S$ nanoparticles. TGA measurement was further carried out to check the percentage of $Fe_{1-x}S$ in the composites as shown in Fig. S4. From 300 ^oC to 650 ^oC, $Fe_{1-x}S$ was oxidized to Fe_2O_3 slowly, while the MC was burned to CO_2. Thus, it validates that $Fe_{1-x}S$ accounts for 64 wt.% of the $Fe_{1-x}S$-MC nanocomposites.

Raman spectrum collected from the MC sample (Fig. 2g) displayed two strong peaks at 1585 and 1346 cm^{-1}. The G band at 1585 cm^{-1} can be assigned to the characteristic doubly degenerate E_{2g} mode of graphite, resulting from the emission of zone-central optical phonons.[18-20] The explicit D band at 1346 cm^{-1} is possibly associated with the defects in

graphite referring to the modes coming approximately from the K point of graphite.[21, 22] More specifically, the D peak is possibly due to the LO phonons around K,[23] which is activated by double resonance[24, 25] and strongly dispersive with excitation energy due to the Kohn Anomaly at K.[25-27] The intensity of the G band is a bit higher than the D band ($I_D/I_G \approx 0.97$), suggesting that the graphitization of the as-synthesized MC sample is higher than the commercially used carbon fiber papers, carbon cloth or even carbon nanotubes reported in the previously literatures.[28-30] Furthermore, a very broad peak centered at ~2700 cm^{-1} was observed, indicating that the wall of MC consisted of stacked carbon multilayers, similar to the previously reported 3D foothill-like graphene scaffold.[31]

The XRD patterns collected on the MC sample (Fig. S5) exhibited two well-defined broad diffraction peaks which are assigned to the (002) and (100) planes of hexagonal carbon (JCPDS Card No. 41-1487). The broad width of these two peaks indicates that the grain size of the graphite is quite small,[10, 32] even though the MC sample was obtained from high temperature treatment up to 1000 ^oC. Further XRD studies of the as-synthesized hydrothermal product, $Fe_{1-x}S$, and $Fe_{1-x}S$-MC (Fig. 2h) revealed that a Fe-containing middle product was created after the hydrothermal reaction, which is denoted as "as-synthesized HT product". The morphology of the as-synthesized HT product was shown in Figure S6a. It can be clearly seen that nanoparticles were uniformly dispersed on the MC surface. However, no diffraction peak can be clearly identified from the XRD pattern of the as-synthesized HT product, implying the possibility that the as-synthesized HT product is amorphous. After further sulfurization treatment, the final product of $Fe_{1-x}S$-MC was achieved. Strong peaks at 29.9^o, 33.8^o, 43.7^o and 53.1^o were observed (Fig. 2h) which can be indexed to (200), (205), (2010) and (220) planes of the pyrrhotite-5T $Fe_{1-x}S$ (JCPDS Card No. 29-0724), respectively. Note

that due to the strong peak intensity of $Fe_{1-x}S$, there are no obvious peaks from microporous carbon. For comparison, pure $Fe_{1-x}S$ was also synthesized following the same procedure without adding microporous carbon during the reaction process. The XRD pattern of $Fe_{1-x}S$ (Fig. 2h, blue curve) displayed the same peaks as $Fe_{1-x}S$-MC, suggesting that the obtained $Fe_{1-x}S$ was also pyrrhotite-5T $Fe_{1-x}S$. The SEM study (Fig. S6b) reveals that the as-synthesized $Fe_{1-x}S$ particles agglomerated together forming clusters of irregularly shapes.

The TEM examination (Fig. 3a) confirms the presence of thin carbon sheets in microporous carbon, consistent with the SEM observation (Fig. S1). A typical TEM image of the $Fe_{1-x}S$-MC composite was depicted in Fig. 3b, showing numerous nanoparticles assembled on the microporous carbon sheet. Although the sample has been ultrasonically treated for a long time during the TEM sample preparation process, the $Fe_{1-x}S$ particles remained attached, suggesting that the strong bonding between the $Fe_{1-x}S$ particles and the microporous carbon scaffold. The selected area electron diffraction (SAED) pattern measured on the $Fe_{1-x}S$ particles (inset of Fig. 3b) revealed their polycrystalline nature. The diffraction rings from center to outside could be assigned to (220), (2010), (205), and (200), in good agreement with the XRD findings. The high-resolution TEM (HRTEM) image of the $Fe_{1-x}S$ nanoparticle grown on the microporous carbon sheet (Fig. 3c) displayed well-resolved periodic lattice fringe with an interplanar distance of 0.29 nm corresponding to the (220) planes in pyrrhotite-5T Fe_{1-x} S. For comparison, the pure $Fe_{1-x}S$ agglomerates were dispersed by intense ultrasonic treatment for a long time and then studied under the TEM (Fig. 3d), where the irregular $Fe_{1-x}S$ clusters were observed. Their SAED pattern (inset of Fig. 3d) showed exactly the same diffraction rings as the $Fe_{1-x}S$ nanoparticle in $Fe_{1-x}S$-MC, verifying again that the $Fe_{1-x}S$

nanoparticles in $Fe_{1-x}S$-MC are of the same phase as pure $Fe_{1-x}S$, in spite of the different morphologies.

XPS was employed to analyze the valence states of $Fe_{1-x}S$-MC. The survey spectrum (Fig. 4a) shows signals from ion, oxygen, carbon and indium (from the sample holder) . The oxygen signal was ascribed to the attached epoxy groups (C-O), carbonyl groups (C=O), and carboxyl groups (COOH), which were identified in the C 1S spectrum (Fig. 4b) at 286.4eV, 288.4 eV and 288.9eV, respectively.[33, 34] It should be pointed out that the as-carbonized microporous carbon was highly hydrophobic, so they needed to be surface modified with polar functional groups so that the ionic nanoparticles could be successfully grown on it. That is why the as-carbonized microporous carbon was treated in H_2SO_4/HNO_3 to produce the desired oxygen-containing surface functional groups whose presence was indicated by the C 1s spectrum (Fig. 4b). The microporous carbon was found to keep the same morphology after the acid treatment (Fig. S7a-b). The S 2p XPS spectrum of $Fe_{1-x}S$-MC exhibits two peaks at 163.2 and 168.7 eV corresponding to S $2P_{3/2}$ and S $2P_{1/2}$, respectively, which are characteristic features of $Fe_{1-x}S$. The Fe 2P XPS spectrum (Fig. 4d) shows two peaks at 711.4 and 724.8 eV attributable to Fe $2P_{2/3}$ and Fe $2P_{1/2}$, in good agreement with the $Fe_{1-x}S$ phase.

To examine its capability in lithium storage, the acid-treated MC was assembled into a coin-type half-cell, in which Li metal foils are used as the counter electrode. The galvanostatic discharge/charge test was carried out at a current density of 0.33C (1C = 372 mA g^{-1}) between 0 and 3 V *vs*. Li^+/Li. The discharge/charge voltage profile for the 1st, 2nd, 3rd, 20th, 50th, 60th cycles was disclosed in Fig. 5a. Different from the long plateau after 0.5 V observed on graphite in literature,[35] the first discharge profile of MC presents a short voltage plateau at ~1.45 V, and then a long slop starting at ~ 1 V, which is similar to the

voltage profile behavior of functionalized graphene nanoribbon previously reported,[34] suggesting that more than one lithium storage mechanisms were involved. The MC delivers a specific discharge capacity of 552 mAh g^{-1} and a specific charge capacity of 324 mAh g^{-1} in these initial processes. The irreversible capacity of 228 mAh g^{-1} could be caused by the formation of the a solid electrolyte interface (SEI) layer on the surface of MC.[36] Because Li^+ is quite active in the first cycle which induces electrode instability, only 80-90% lithium was recovered in the first extraction process.[35] Furthermore, an SEI layer may be formed during the first cycle due to the electrolyte decomposition that passivates the electrode by allowing only the transportation of ions (e.g., Li^+) but not electrons.[37, 38] After the first cycle, the charging curves of the 2nd, 3rd, 20th well overlapped with each other, whereas the 60th cycle delivered an increased charging capacity. Further long-term cycling test (Fig. 5b) shows that the discharge capacity of MC did not show any decline since the second cycle (300 mAh g^{-1}) and reached 311 mAh g^{-1} after 120 cycles. Excellent coulombic efficiency was also observed on MC after the first 5 cycles (efficiency of 58.5% for the 1st cycle) with the average value over 99.4%. These observations on MC represents a very attractive LIB performance among the carbon material reported to date, *c.f.,* the initial values of hard carbon anodes are usually below 55% due to the formation of a thick SEI layer.[39] Notably, the specific capability (311 mAh g^{-1}) delivered by MC at 0.33C is much higher than the commercial graphite (normally at 150-200 mAh g^{-1} at 0.33C).[40] Previous research has pointed out that the major drawback of graphite as LIB anode materials is limited by its low theoretical capacity of 372 mAh g^{-1}, calculated assuming that the LiC_6 compound is formed for lithium storage.[35] For MC studied here, the observed high lithium storage capability is possibly due to other lithium storage mechanisms, e.g., surface Li storage.[41] Researchers have proposed that the formation of

lithium multilayers on carbon surface is an intermediate state between lithium intercalation and reduction to metallic lithium, which can be imaged as the lithium plating onto the carbon surface at the electrode potential close to that of the elemental lithium, resulting in additional lithium ions converted to metallic lithium.[41, 42]

For comparison, the cycling performance of the reduced graphene oxide (RGO) from literature [43] under the same current density was drawn in Fig. 5(b), which shows nearly the same specific capacity (316 mAh g^{-1} at 50^{th} cycle). In spite of the encouraging battery performance achieved, the energy density of the sugarcane waste-derived MC is still far to meet the ever-increasing demand in mobile electronics industry and large-scale applications. In order to boost the energy density, different strategies can be implemented, such as, integrations with functional metal oxides (Fe_3O_4, CuO_2, TiO_2, SnO_2, etc.),[43-46] doping with active elements (B, N and S),[47-49] and tailoring the surface functional group.[34] Herein, we utilize a novel sulfurization method to grow pyrrhotite-5T $Fe_{1-x}S$ nanoparticles on MC to boost its energy density. Our interest in the $Fe_{1-x}S$ modification strategy are based on the fact that sulfides possess high theoretical capacities, and are non-toxic and cost effective.[50, 51] Nonetheless, sulfide suffers large volume charge upon lithium uptake and release, and the formation of the insulating polysulfide Li_2S_x ($1<x<8$)[52] which is soluble in the liquid electrolyte and can gradually migrate to the cathode, causing severe loss of the active materials and poor cycling stability. Furthermore, the dissolved polysulfides can also deteriorate the conductivity of the electrolyte by forming an insulating layer outside the electrode, leading to the capacity degradation.[53, 54] Recently, it was found that reducing the particle size of sulfides or wrapping them with a thin carbon layer could be an effective strategy in alleviating the dissolution problem of polysulfide.[51, 55, 56] Here, a novel type of

nanocomposite of iron sulfide nanoparticles and 3D MC can be very promising for achieving high-performance LIBs.

The cycling performance of the $Fe_{1-x}S$-MC nanocomposite was tested at a current density of 100 mA g^{-1} (Fig. 6a). Different from the decay behaviors commonly observed on FeS-related electrodes in previous studies,[57] $Fe_{1-x}S$-MC delivers stable capability in the first 100 cycles, and keeps increasing in the following cycles. At the first cycle, $Fe_{1-x}S$-MC deliver an initial discharge capacity of 1094 mAh g^{-1} and a charge capacity of 787 mAh g^{-1}, leading to a Coulombic efficiency of 72%. The great discharging/charging capacity much higher than the theoretical value (609 mAh g^{-1} for FeS) is possibly due to the formation of the specific SEI layer upon decomposition of the electrolyte solvent.[43, 58, 59] Note that extra high capacity has been widely observed in transition metal oxide electrodes, which was suggested to be due to the formation of a gel-like organic layer on the surface of the porous architectures.[55, 60] At the second cycle, $Fe_{1-x}S$-MC delivers a discharge capacity of 788 mAh g^{-1} and charge capacity of 745 mAh g^{-1}, showing a quickly increased Coulombic efficiency to 94%. After 200 cycles, the capacity gradually increased to 1185 mAh g^{-1}, which is more than 3 times of the commercial used graphite (372 mAh g^{-1}). To the best of our knowledge, this is the highest value among the iron sulfide-based materials reported to date (Fig. 7 and Table S1).[50, 51, 57, 61-65] The SEM image of $Fe_{1-x}S$-MC nanocomposites after cycling at 100 mA g^{-1} for ~200 cycles (Fig. S8) reveals a varied morphology due to the formation of SEI layer on the surface. However, remarkably, the $Fe_{1-x}S$ particles were still decorated on MC even after extended cycling with Li^+ uptake and release, indicating the helpful role of MC in preserving the sulfide materials during cycling.

For comparison, the cycling performance of pure $Fe_{1-x}S$ electrodes was tested at 100 mA g^{-1}, which showed a poor cyclability (Fig. 6a). Although the initial discharge capacity (1219 mAh g^{-1}) is higher than $Fe_{1-x}S$-MC, it kept decreasing in the first 20 cycles, and quickly dropped to 235 mAh g^{-1} after 60 cycles. The poor cycling stability of the pure $Fe_{1-x}S$ particles is possibly due to formation of the undesirable polysulfide from $Fe_{1-x}S$, the volume expansion of the sulfide, and the aggregation of the nanoparticles during the continuous Li^+ uptake and release process. This result confirms the important role of MC, which helps alleviate the sulfide aggregation, prevent polysulfide dissolution, and increase the conductivity of the whole composites.

Figure 6b shows the charging/discharging voltage profiles of the $Fe_{1-x}S$-MC nanocomposites electrode for 1th, 2nd, 3rd, 20th, 50th, and 100th at a current density of 100 mA g^{-1} in the voltage range of 0 to 3V *vs.* Li^+/Li. In the first discharge process, a large plateau at ~ 1.3V was seen, which is assigned to the reaction between $Fe_{1-x}S$ and lithium with the formation of Fe, Li_2S and Li-rich phases.[52,66] A slope between 0.8 and 0.2V was observed, which is attributed to the formation of the SEI layer and Li_2FeS_2 (eq. 1) .[51, 61]

$$Fe_{1-x}S+2Li+2e^{-}\rightarrow Li_2FeS_2+Fe \qquad (1)$$

Note that the conversion between $Li_2.xFeS_2$ and Li_2FeS_2 is reversible, allowing the application of iron sulfides for rechargeable LIBs. In the charging process, an obvious voltage plateau was observed between 1.8-1.9 V (Fig. 6b), which is attributed to the oxidation process of Fe to Li_2FeS_2.[61] From the 2nd to 20th cycles, nearly the same lithiation/delithiation profiles were observed, presenting stable cycling performance. It is noticed that the 50th cycle delivered higher discharge capacity than the previous cycles, and even higher capacities were delivered after the 100th cycle, consistent with the its cycling performance shown in Fig. 6a.

In order to evaluate their capability for high powerful density LIBs, the $Fe_{1-x}S$-MC nanocomposites were galvanostatically tested at various current densities from 100 mA g^{-1} to 8000 mA g^{-1} (Fig. 6c). Excellent rate capability was observed on $Fe_{1-x}S$-MC: the discharge capacities were 776, 728, 715, 669, 562, and 361 mAh g^{-1} at 100, 300, 500, 1000, 4000, and 8000 mA g^{-1}, respectively. Remarkably, after sixty cycles with different current densities up to 8000 mA g^{-1}, a high capacity of 755 mAh g^{-1} was successfully recovered with the current density shifted back to 100 mA g^{-1}. For comparison, the rate performance of pure $Fe_{1-x}S$ particles delivered discharge capacities of 826, 773, 735, 650, 408, and 232 mAh g^{-1} at 100, 300, 500, 1000, 4000, and 8000 mA g^{-1}, respectively. It can be seen that, although the $Fe_{1-x}S$ particle electrode delivered higher specific capacities than $Fe_{1-x}S$-MC at the low current densities (100 and 300 mA g^{-1}), it showed significantly lower specific capacities with much worse stability at the high current densities (1000, 4000, and 8000 mA g^{-1}). This observation is consistent with the cycling behaviors depicted in Fig. 6a.

The cycling performances of $Fe_{1-x}S$-MC and pure $Fe_{1-x}S$ at the high current density of 300 mA g^{-1} were further investigated (Fig. 6d). The capacity of $Fe_{1-x}S$-MC decreased in the initial 10 cycles and then became stabilized afterwards, delivering a discharge capacity of 941, 662, and 630 mAh g^{-1} at the 1st, 10th and 40th cycle, respectively. On the other hand, with capacity measured to be 959, 720, and 333 mAh g^{-1} at the 1st, 10th and 40th cycle, respectively, the pure $Fe_{1-x}S$ delivered a slightly higher capacity than $Fe_{1-x}S$-MC in the initial 20 cycles but its performance deteriorated quickly afterwards, in good agreement with the cycling performance at 100 mA g^{-1} shown in Fig. 6a. The largely improved rate and cycling performance of $Fe_{1-x}S$-MC is mainly attributed to the synergetic effects of the $Fe_{1-x}S$ nanostructures and the hierarchical MC framework. The well dispersed $Fe_{1-x}S$ nanoparticles

are more tolerant to the large volume change associated with the lithium uptake and release process. The strong bonding between the $Fe_{1-x}S$ nanoparticles and the MC substrate may help alleviate the formation of the insulated polysulfide Li_2S_x.[50] Meanwhile, MC serves as a flexible and robust conductive scaffold that better accommodates the strain induced during the lithiation/delithiation process while maintaining the good electrical contact with the $Fe_{1-x}S$ nanoparticles. Furthermore, by evenly dispersing the $Fe_{1-x}S$ nanoparticles on MC, self-aggregation of the $Fe_{1-x}S$ nanoparticles can be effectively restricted during the cycling process, while easy accessibility by the electrolyte is ensured with the active materials present in a 3D open hierarchical architecture with a large work surface area.

To better understand the redox reaction taking place during the Li^+ uptake and release process, a cyclic voltammetry (CV) study of $Fe_{1-x}S$-MC was carried out between 3 and 0 V (Fig. 6e). A sharp reduction peak at *ca*. 1.03 V was observed in the first cycle, attributed to the following reaction (eq. 2):[50-52]

$$Fe_{1-x}S + 2Li + 2e^- \rightarrow Li_2S + Fe \qquad (2)$$

Another broad discernible reduction peak at 0.4 - 0.8 V shown in the first cycle was assigned to the formation of the SEI layer,[50] which disappeared in the subsequent charge/discharge cycles. A strong anodic peak at 1.95 V was found in the first cycle, which is ascribed to the oxidation of Fe to $Li_{2-}xFeS_2$.[62, 67] In the later cycles (2nd and 3rd cycles), two reduction peaks appeared at 1.36 and 1.91 V, indicating the formation of $Li_{2-}xFeS_2$[51, 62] and the reversible delithiation process ($Li_{2-}xFeS_2$ to Li_2FeS_2).[50]

The AC impedance measurements were conducted on $Fe_{1-x}S$-MC and $Fe_{1-x}S$ to understand their interfacial properties. The Nyquist plots (Fig. 8a) of $Fe_{1-x}S$-MC and $Fe_{1-x}S$ both showed a semicircular loop at high frequency and a sloping straight line at low frequency.

The analysis of the equivalent circuit model (Fig. 8b) is given as follows: a) Ohmic resistance *Rs* is related to Li^+ transport in the electrolyte; b) the resistance R_f and a constant phase element (CPE) 1 corresponds to Li^+ migration through the surface layers; c) the resistance R_{ct} and a CPE2 is associated with the charge transfer between the electrode/electrolyte interface; d) a Warburg impedance *W* is attributed to Li^+ diffusion in active material.[68-70] Figure 7a clearly reveals that R_{ct} value of $Fe_{1-x}S$-MC and $Fe_{1-x}S$ was ~ 50 and 125 Ω, respectively, implying that the improvement in the electronic conductivity of $Fe_{1-x}S$-MC is due to the combination of $Fe_{1-x}S$ with MC. These results confirm that the 3D hierarchical MC can serve as a highly conductive network for effectively improving electron transport throughout the nanocomposites.

Conclusion

In summary, a scalable method has been introduced for conveniently transforming sugarcane waste into hierarchical microporous carbon (MC) for lithium-ion battery applications. Microporous carbon thus obtained exhibits a comparable storage capability to reduced graphene oxide, far better than the current commercial graphite. To further improve the lithium storage capability, $Fe_{1-x}S$ nanoparticles were deposited on the microporous carbon scaffold robustly using a novel sulfurization method. The as-prepared hierarchical composite electrode of $Fe_{1-x}S$-MC delivers excellent cycling stability, good rate retention, and a capacity well beyond the theoretical value. The superior performance of $Fe_{1-x}S$-MC can be ascribed to the synergetic effects from the high flexibility high conduction of the MC scaffolds, and the nanosized $Fe_{1-x}S$. This work demonstrates the great potential of biological waste as a rich recyclable resource for supplying sustainable and cost-effective solutions to energy challenges.

Acknowledgements

This work was supported by National Natural Science Foundation of China (NSFC Grants Nos. 51502099, 51402344, 51571096 and 51202206), National Key Basic Research Program of the Chinese Ministry of Science and Technology (Grant 2012CB932203), the City University of Hong Kong (Project No. 7004192), and the Centre for Functional Photonics at the City University of Hong Kong. C.D.W. acknowledges the start research foundation from Huazhong University of Science and Technology.

Notes and references

1. J.-M. Tarascon, *Philos. Trans. R. Soc. London*, 2010, **368**, 3227-3241.

2. J.-M. Tarascon and M. Armand, *Nature*, 2001, **414**, 359-367.

3. Y. Su, S. Li, D. Wu, F. Zhang, H. Liang, P. Gao, C. Cheng and X. Feng, *Acs Nano*, 2012, 6, 8349-8356.

4. S. Li, D. Wu, C. Cheng, J. Wang, F. Zhang, Y. Su and X. Feng, *Angew. Chem. Int. Ed.*, 2013, **125**, 12327-12331.

5. B. Scrosati, J. Hassoun and Y.-K. Sun, *Energy Environ. Sci.*, 2011, **4**, 3287-3295.

6. A. Yoshino, *Angew. Chem. Int. Ed.*, 2012, **51**, 5798-5800.

7. B. Kang and G. Ceder, *Nature*, 2009, **458**, 190-193.

8. V. G. Pol and M. M. Thackeray, *Energy Environ. Sci.*, 2011, **4**, 1904-1912.

9. J. B. Goodenough, *Energy Environ. Sci.*, 2014, **7**, 14-18.

10. J. Jiang, J. Zhu, W. Ai, Z. Fan, X. Shen, C. Zou, J. Liu, H. Zhang and T. Yu, *Energy Environ. Sci.*, 2014, **7**, 2670-2679.

11. D. S. Jung, M.-H. Ryou, Y. J. Sung, S. B. Park and J. W. Choi, *Proc. Natl. Acad. Sci. U.S.A.*, 2013, **110**, 12229-12234.

12. D. Tilman, K. G. Cassman, P. A. Matson, R. Naylor and S. Polasky, *Nature*, 2002, **418**, 671-677.

13. R. Kumar, D. Verma, B. L. Singh and U. Kumar, *Bioresour. Technol.*, 2010, **101**, 6707-6711.

14. M. A. Arbex, L. C. Martins, R. C. de Oliveira, L. A. A. Pereira, F. F. Arbex, J. E. D. Cançado, P. H. N. Saldiva and A. L. F. Braga, *J Epidemiol Community Health*, 2007, **61**, 395-400.

15. F. S. Silva, J. Cristale, P. A. André, P. H. Saldiva and M. R. Marchi, *Atmos. Environ.*, 2010, **44**, 5133-5138.

16. A. Jain, S. Tripathi, *J. Energy Storage*, 2015, http://dx.doi.org/10.1016/j.est.2015.09.010

17. C.-H. Huang, R.-A. Doong, *Microporous Mesoporous Mater.,* 2012,**147**, 47-52.

18. J. Qin, C. He, N. Zhao, Z. Wang, C. Shi, E.-Z. Liu and J. Li, *ACS nano*, 2014, **8**, 1728-1738.

19. W. Qian, X. Cui, R. Hao, Y. Hou and Z. Zhang, *ACS Appl. Mater. Interfaces*, 2011, **3**, 2259-2264.

20. C. Wang, M. F. Yuen, T. W. Ng, S. K. Jha, Z. Lu, S. Y. Kwok, T. L. Wong, X. Yang, C. S. Lee and S. T. Lee, *Appl. Phys. Lett.*, 2012, **100**, 253107.

21. C. Wang, Y. Zhou, L. He, T.-W. Ng, G. Hong, Q.-H. Wu, F. Gao, C.-S. Lee and W. Zhang, *Nanoscale*, 2013, **5**, 600-605.

22. S. Reich and C. Thomsen, *Philos. Trans. Roy. Soc. London Ser. A*, 2004, **362**, 2271-2288.

23. A. C. Ferrari and J. Robertson, *Phys. Rev. B: Condens. Matter*, 2000, **61**, 14095.

24. A. Baranov, A. Bekhterev, Y. S. Bobovich and V. Petrov, *Opt. Spektrosk*, 1987, **62**, 1036.

25. C. Thomsen and S. Reich, *Phys. Rev. Lett.*, 2000, **85**, 5214.

26. S. Piscanec, M. Lazzeri, F. Mauri, A. Ferrari and J. Robertson, *Phys. Rev. Lett.*, 2004, **93**, 185503.

27. A. C. Ferrari, *Solid State Commun.*, 2007, **143**, 47-57.

28. J. Chen, J. Z. Wang, A. I. Minett, Y. Liu, C. Lynam, H. Liu and G. G. Wallace, *Energy Environ. Sci.*, 2009, **2**, 393-396.

29. N. Padmanathan and S. Selladurai, *RSC Adv.*, 2014, **4**, 8341-8349.

30. E. Steven, W. R. Saleh, V. Lebedev, S. F. Acquah, V. Laukhin, R. G. Alamo and J. S. Brooks, *Nat. Commun.*, 2013, **4**.

31 C. Wang, J. Xu, M. F. Yuen, J. Zhang, Y. Li, X. Chen and W. Zhang, *Adv. Funct. Mater.*, 2014, **24**, 6372-6380.

32. W. E. Tenhaeff, O. Rios, K. More and M. A. McGuire, *Adv. Funct. Mater.*, 2014, **24**, 86-94.

33. A. L. Higginbotham, D. V. Kosynkin, A. Sinitskii, Z. Sun and J. M. Tour, *ACS nano*, 2010, **4**, 2059-2069.

34. C. Wang, Y.-S. Li, J. Jiang and W.-H. Chiang, *ACS Appl. Mater. Interfaces*, 2015, **7**, 17441-17449.

35. N. A. Kaskhedikar and J. Maier, *Adv. Mater.*, 2009, **21**, 2664-2680.

36. V. Eshkenazi, E. Peled, L. Burstein and D. Golodnitsky, *Solid State Ionics*, 2004, **170**, 83-91.

37. E. Peled, *J. Electrochem. Soc.*, 1979, **126**, 2047-2051.

38. K. Xu, *Chem. Rev.*, 2004, **104**, 4303-4418.

39. B. Guo, J. Shu, K. Tang, Y. Bai, Z. Wang and L. Chen, *J. Power Sources*, 2008, **177**, 205-210.

40. E. Yoo, J. Kim, E. Hosono, H.-s. Zhou, T. Kudo and I. Honma, *Nano Lett.*, 2008, **8**, 2277-2282.

41. M. Deschamps and R. Yazami, *J. Power Sources*, 1997, **68**, 236-238.

42. R. Yazami and M. Deschamps, *J. Power Sources*, 1995, **54**, 411-415.

43. C. Wang, Q. Zhang, Q.-H. Wu, T.-W. Ng, T. Wong, J. Ren, Z. Shi, C.-S. Lee, S.-T. Lee and W. Zhang, *RSC Adv.*, 2012, **2**, 10680-10688.

44. C. Wang, J. Xu, R. Ma and M.-F. Yuen, *Mater. Chem. Phys.*, 2014, **148**, 411-415.

45. L. He, C. Wang, X. Yao, R. Ma, H. Wang, P. Chen and K. Zhang, *Carbon*, 2014, **75**, 345-352.

46. H. Wang, H. Huang, C. Niu and A. L. Rogach, *Small*, 2015, **11**, 1364-1383.

47. X. Ren, J. Zhu, F. Du, J. Liu and W. Zhang, *J. Phys. Chem. C* , 2014, **118**, 22412-22418.

48. F. Zheng, Y. Yang and Q. Chen, *Nat. Commun.*, 2014, **5**, 5261.

49. Z. Ma, S. Dou, A. Shen, L. Tao, L. Dai and S. Wang, *Angew. Chem. Int. Ed.*, 2015, **127**, 1908-1912.

50. C. Xu, Y. Zeng, X. Rui, N. Xiao, J. Zhu, W. Zhang, J. Chen, W. Liu, H. Tan and H. H. Hng, *ACS nano*, 2012, **6**, 4713-4721.

51. B. Wu, H. Song, J. Zhou and X. Chen, *Chem. Commun.*, 2011, **47**, 8653-8655.

52. Y. Kim and J. B. Goodenough, *J. Phys. Chem. C*, 2008, **112**, 15060-15064.

53. L. Ji, M. Rao, S. Aloni, L. Wang, E. J. Cairns and Y. Zhang, *Energy Environ. Sci.*, 2011, **4**, 5053-5059.

54. L. Ji, M. Rao, H. Zheng, L. Zhang, Y. Li, W. Duan, J. Guo, E. J. Cairns and Y. Zhang, *J. Am. Chem. Soc.*, 2011, **133**, 18522-18525.

55. J. Zhou, H. Song, X. Chen, L. Zhi, S. Yang, J. Huo and W. Yang, *Chem. Mat.*, 2009, **21**, 2935-2940.

56. R. Cakan, *Chem. Commun.*, 2008, 3759-3761.

57. L. Fei, Q. Lin, B. Yuan, G. Chen, P. Xie, Y. Li, Y. Xu, S. Deng, S. Smirnov and H. Luo, *ACS Appl. Mater. Interfaces*, 2013, **5**, 5330-5335.

58. Y. Wang, F. Su, J. Y. Lee and X. Zhao, *Chem. Mat.*, 2006, **18**, 1347-1353.

59. H. Liu, G. Wang, J. Wang and D. Wexler, *Electrochem. Commun.*, 2008, **10**, 1879-1882.

60. S. Jin, H. Deng, D. Long, X. Liu, L. Zhan, X. Liang, W. Qiao and L. Ling, *J. Power Sources*, 2011, **196**, 3887-3893.

61. X. Wang, Q. Xiang, B. Liu, L. Wang, T. Luo, D. Chen and G. Shen, *Sci. Rep.*, 2013, **3**, 2007.

62. B.-C. Kim, K. Takada, N. Ohta, Y. Seino, L. Zhang, H. Wada and T. Sasaki, *Solid State Ionics*, 2005, **176**, 2383-2387.

63. C. Xing, D. Zhang, K. Cao, S. Zhao, X. Wang, H. Qin, J. Liu, Y. Jiang and L. Meng, *J. Mater. Chem. A*, 2015, **3**, 8742-8749.

64. E. Shangguan, F. Li, J. Li, Z. Chang, Q. Li, X.-Z. Yuan and H. Wang, *J. Power Sources*, 2015, **291**, 29-39.

65. K. Zhang, T. Zhang, J. Liang, Y. Zhu, N. Lin and Y. Qian, *RSC Adv.*, 2015, **5**, 14828-14831.

66. Y. Shao-Horn and Q. C. Horn, *Electrochim. Acta*, 2001, **46**, 2613-2621.

67. D. Golodnitsky and E. Peled, *Electrochim. Acta*, 1999, **45**, 335-350.

68. R. Ma, Z. Lu, C. Wang, H.-E. Wang, S. Yang, L. Xi and J. C. Chung, *Nanoscale*, 2013, **5**, 6338-6343.

69. L. J. Xi, H.-E. Wang, Z. G. Lu, S. L. Yang, R. G. Ma, J. Q. Deng and C. Y. Chung, *J. Power Sources*, 2012, **198**, 251-257.

70. J.-Z. Kong, C. Ren, G.-A. Tai, X. Zhang, A.-D. Li, D. Wu, H. Li and F. Zhou, *J. Power Sources*, 2014, **266**, 433-439.

Figures

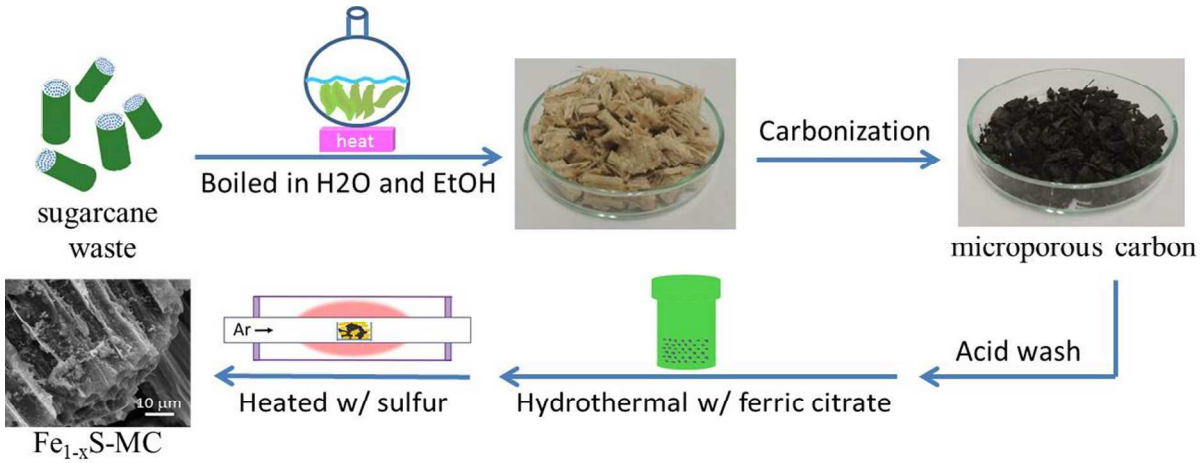

Fig. 1 (a) schematic diagram of disposable sugarcane, (b) cooking treatment of disposable sugarcane pieces, (c) dried sugarcane, (d) microporous carbon, (e) hydrothermal synthesis of the ion precursor-MC composites, (f) sulfurization treatment of the ion precursor-MC composites to obtain $Fe_{1-x}S$ -MC.

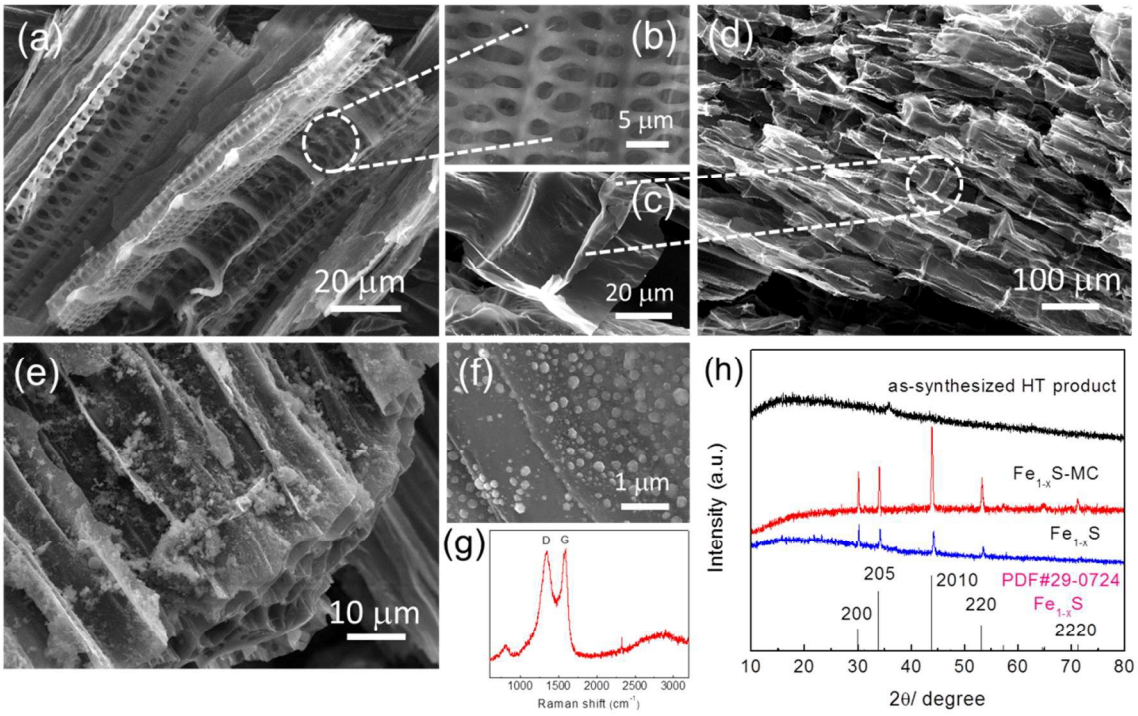

Fig. 2 (a)-(d) SEM images of microporous carbon, (e)-(f) SEM images of $Fe_{1-x}S$-MC composites, (g) Raman spectrum of microporous carbon, (h) XRD patterns of the as-synthesized hydrothermal (HT) product, $Fe_{1-x}S$ and $Fe_{1-x}S$-MC, and the standard XRD pattern of pyrrhotite-5T $Fe_{1-x}S$.

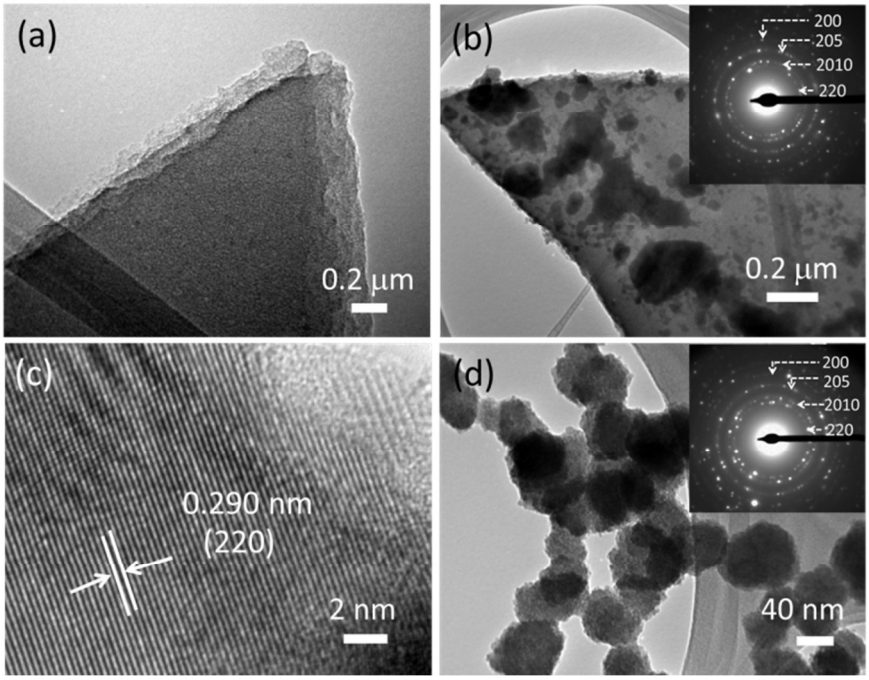

Fig. 3 TEM image of (a) microporous carbon and (b) $Fe_{1-x}S$-MC composites. (c) High-resolution image of $Fe_{1-x}S$ decorated on microporous carbon. (d) TEM image of the pure $Fe_{1-x}S$. The inset of (b) is the SAED of $Fe_{1-x}S$ in the composites, and the inset of (d) is the SAED of pure $Fe_{1-x}S$.

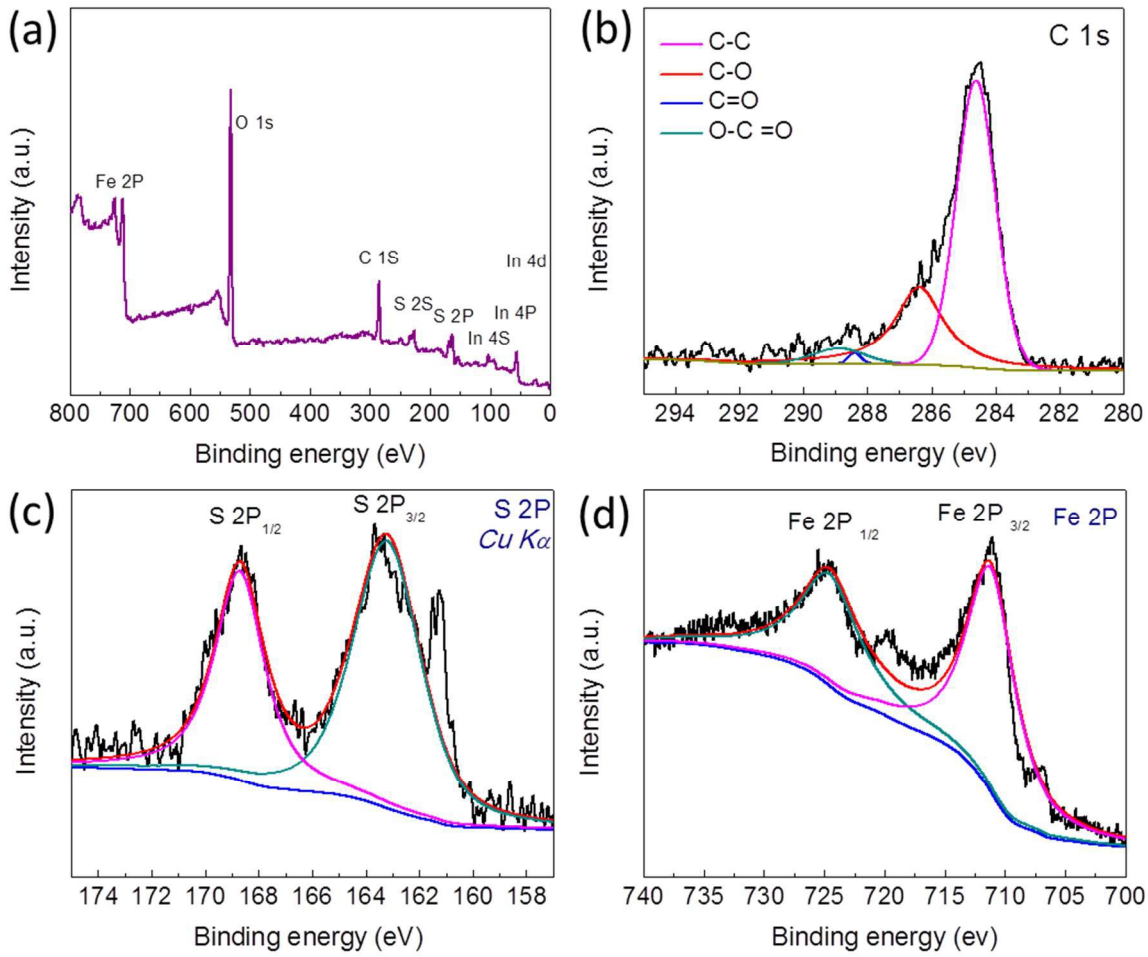

Fig. 4 XPS spectra of the as-synthesized $Fe_{1-x}S$-MC: (a) survey spectra, (b) C 1S, (c) S 2p, and (d) Fe 2p core level spectra.

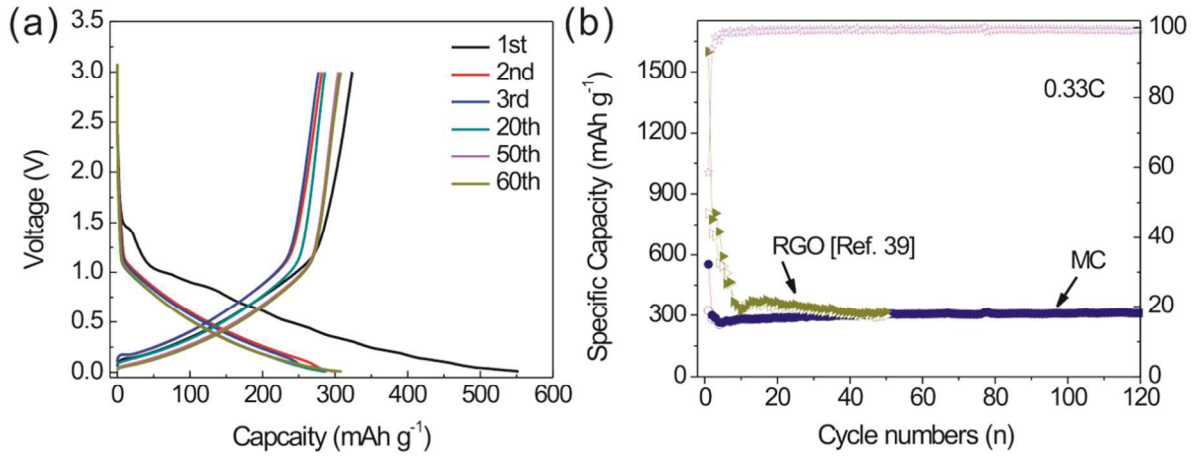

Fig. 5 (a) Galvanostatic voltage profiles of microporous carbon at 0.33C at the 1st, 2nd, 3rd, 20th, 50th, 60th cycles. (a) Cycling performance of the microporous carbon and reduced graphene oxide (RGO) between 0.0 and 3.0 V vs. Li/Li^+ at a current density of 0.33C.

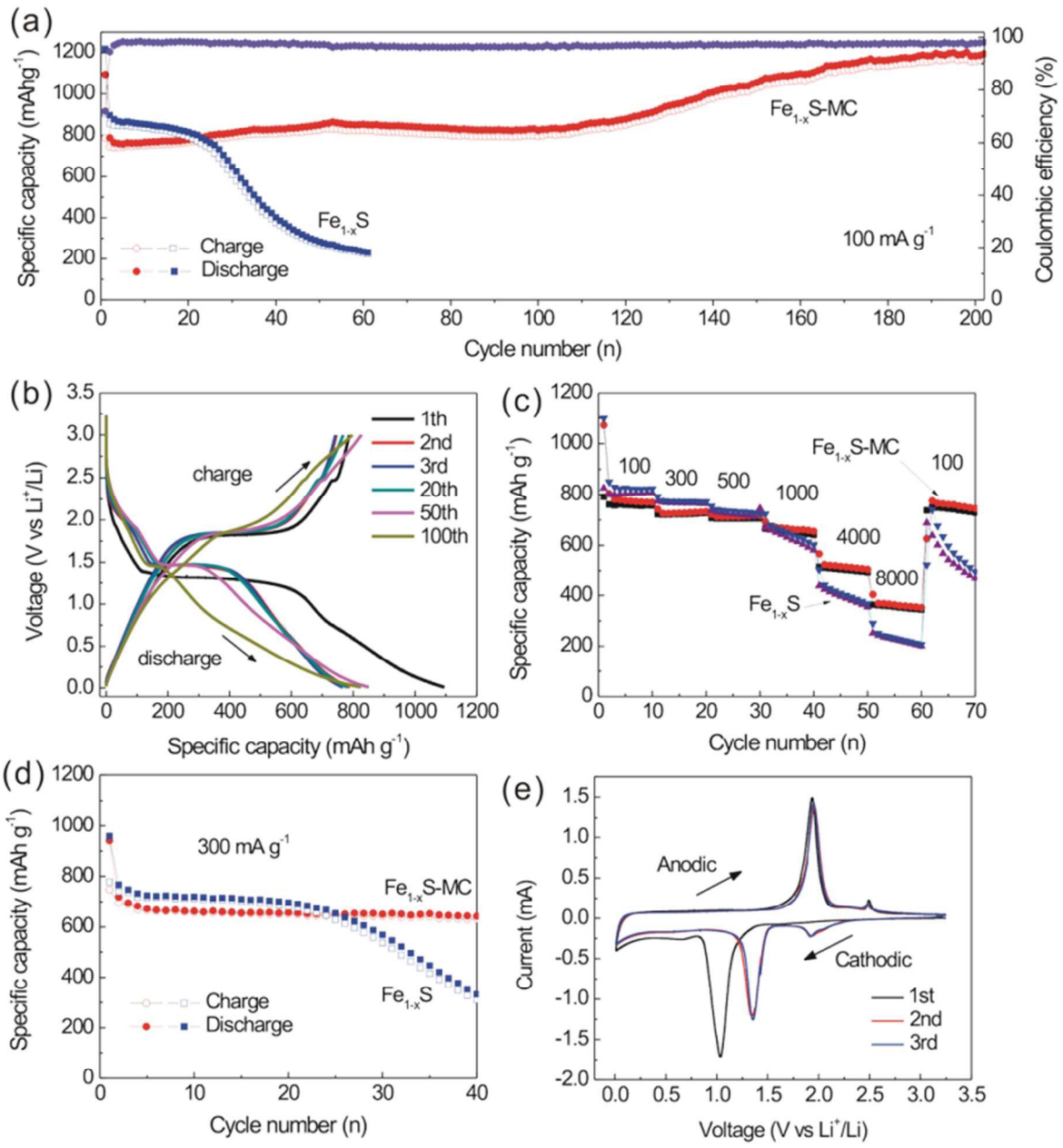

Fig. 6 (a) Cycling performance of the $Fe_{1-x}S$-MC nanocomposites and $Fe_{1-x}S$ at a current density of 100 mA g^{-1}. (b) Voltage profiles of $Fe_{1-x}S$-MC at 1th, 2nd, 3rd, 20th, 50th, at 100 mA g^{-1}. (c) Galvanostatic charge-discharge capacity of the $Fe_{1-x}S$-MC nanocomposites and $Fe_{1-x}S$ at various rates from 100 to 8000 mA g^{-1}. (d) Cycling performance of the $Fe_{1-x}S$-MC nanocomposites and $Fe_{1-x}S$ at a current density of 300 mA g^{-1}. (e) Cyclic voltammograms

(CVs) of the $Fe_{1-x}S$-MC nanocomposites for the initial three cycles at a scan rate of 0.1 mV s^{-1} and a potential range of 0-3 V vs. Li^+/Li.

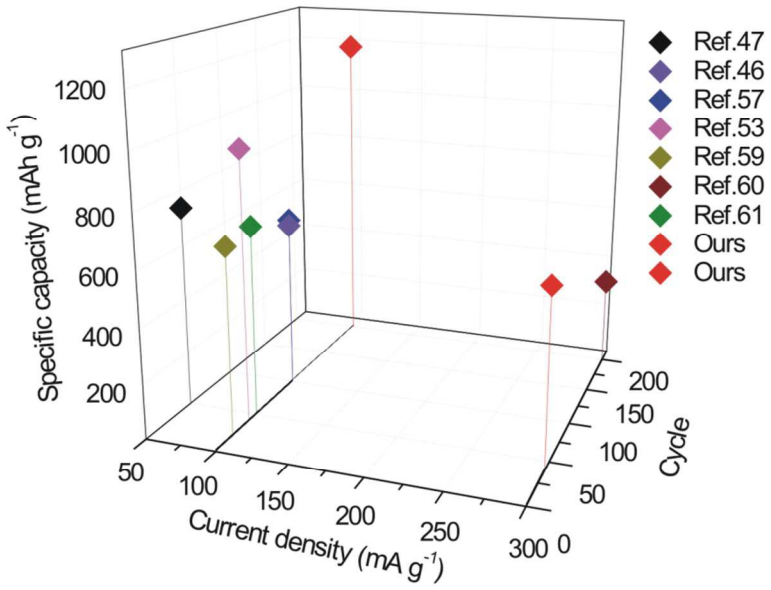

Fig. 7.

Fig. 7 Cycling performance comparison with the previously reported iron sulfide-based LIB anodes tested at constant current densities.

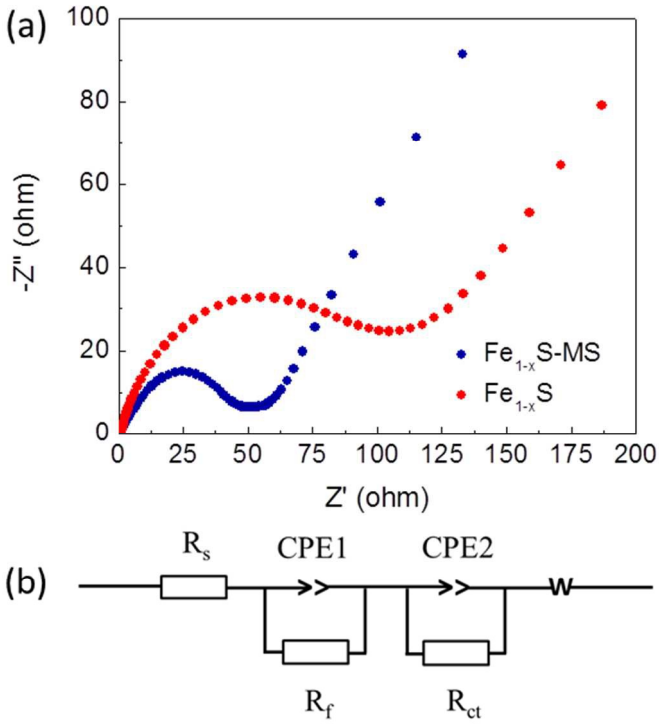

Fig. 8 (a) The Nyquist plots of $Fe_{1-x}S$-MC and $Fe_{1-x}S$. The applied frequency was in the range of 100 kHz to 0.01 Hz with an excitation voltage of 10 mV. (b) Equivalent circuit performed to fit the Nyquist plots in (a).

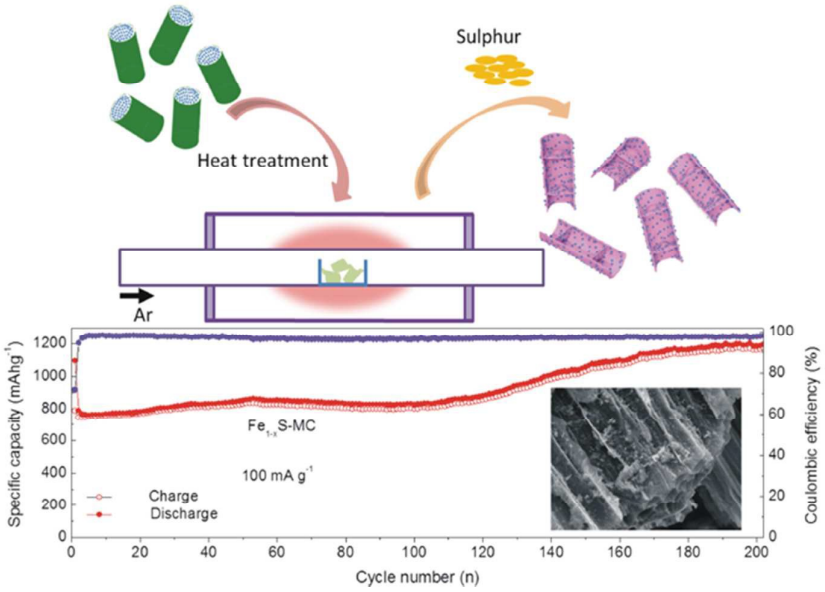

A scalable, green method to prepare microporous carbon from sugarcane waste for superior lithium storage capability of $Fe_{1-x}S$.